Opto-Electronic Advances

Supplementary information

April 2024, Vol. 7, No. 4

DOI: 10.29026/oea.2024.230148

Polariton lasing in Mie-resonant perovskite nanocavity

Mikhail A. Masharin[1,2†], Daria Khmelevskaia[2†], Valeriy I. Kondratiev[2], Daria I. Markina[2], Anton D. Utyushev[2], Dmitriy M. Dolgintsev[2], Alexey D. Dmitriev[2], Vanik A. Shahnazaryan[2,3], Anatoly P. Pushkarev[2], Furkan Isik[1,4], Ivan V. Iorsh[2,5], Ivan A. Shelykh[3,6], Hilmi V. Demir[1,4*], Anton K. Samusev[7*] and Sergey V. Makarov[2,8*]

[1]UNAM-Institute of Materials Science and Nanotechnology, National Nanotechnology Research Center, Department of Electrical and Electronics Engineering, Department of Physics, Bilkent University, Ankara 06800, Turkey; [2]ITMO University, School of Physics and Engineering, St. Petersburg 197101, Russia; [3]Abrikosov Center for Theoretical Physics, MIPT, Dolgoprudnyi, Moscow Region 141701, Russia; [4]LUMINOUS! Center of Excellence for Semiconductor Lighting and Displays, School of Electrical and Electronic Engineering, School of Physical and Mathematical Sciences, School of Materials Science and Engineering, Nanyang Technological University, 639798, Singapore; [5]Department of Physics, Engineering Physics and Astronomy, Queen's University, Kingston, Ontario K7L 3N6, Canada; [6]Science Institute, University of Iceland, Dunhagi 3, IS-107, Reykjavik, Iceland; [7]Experimentelle Physik 2, Technische Universität Dortmund, Dortmund 44227, Germany; [8]Qingdao Innovation and Development Center, Harbin Engineering University, Qingdao 266000, China.

[†]These authors contributed equally to this work.

*Correspondence: HV Demir, E-mail: volkan@fen.bilkent.edu.tr; AK Samusev, E-mail: a.samusev@metalab.ifmo.ru; SV Makarov, E-mail: s.makarov@metalab.ifmo.ru

Supplementary information for this paper is available at https://doi.org/10.29026/oea.2024.230148

Section 1: Experimental measurement of ASE from perovskite thin film under the light cone

As we discuss in the main text, perovskite polycrystalline thin film is able to support waveguide modes, which can be directly measured by angle-resolved spectroscopy with SIL. Angle-resolved emission spectra, measured under femtosecond laser pump at 515 nm at pump fluences around 0.01 mJ/cm² and 1 mJ/cm² in the regime of low coupling of SIL (when the waveguide is located far from the SIL). The waveguide mode is shown in Fig. S1(a) with $k_x/k_0 \approx 1.8$. The low coupling of the SIL provides low radiative optical losses of the waveguide mode. In the case of low pump fluence, we observe a broad intensive PL signal above the light cone and a low-intensive waveguide mode below the light cone. According to our assumptions, in this regime, we measure exciton PL with thermalized polaritons over the branch. At the pump fluences around 1 mJ/cm² above the light cone, ASE emission appears in the spectral region around 2.26 eV. At the same time below the light cone, we also observe an enhancement of the intensity in the same spectral region, corresponding to the ASE. Moreover, the intensity, measured below the light cone strongly exceeds the intensity above. It can be explained as the origin of ASE came from the guided polariton and then it is scattered via defects and film grains, outcoupling to the free space.

In the experiment we also change the distance between SIL and perovskite thin film, changing the SIL coupling efficiency and hence radiative losses of waveguide mode (Fig. S1(b)). In the case of the lowest radiative losses, γ_1 we observe pronounced red broadening of ASE with increasing pump fluence. When we decrease the distance between SIL and film with increased radiative losses γ_2 the red broadening is suppressed. In the regime of the SIL overcoupling with the highest optical losses γ_3 we do not observe any ASE. The phenomenon can be explained in terms of the polariton lifetimes. When we increase radiative losses of guided mode, polaritons recombine or scatter to the lower energies. If losses are too high, polariton concentration cannot achieve a nonlinear regime because of fast recombination, which we observe in the case of γ_3.

We also study light-light curves for different guided polariton radiative losses shown in Fig. S1(c). The ASE provides pronounced threshold behavior in the case of low optical losses. Moreover, the ASE threshold is increasing with increasing waveguide optical losses. As there exists a threshold concentration of polaritons for stimulation, increasing losses

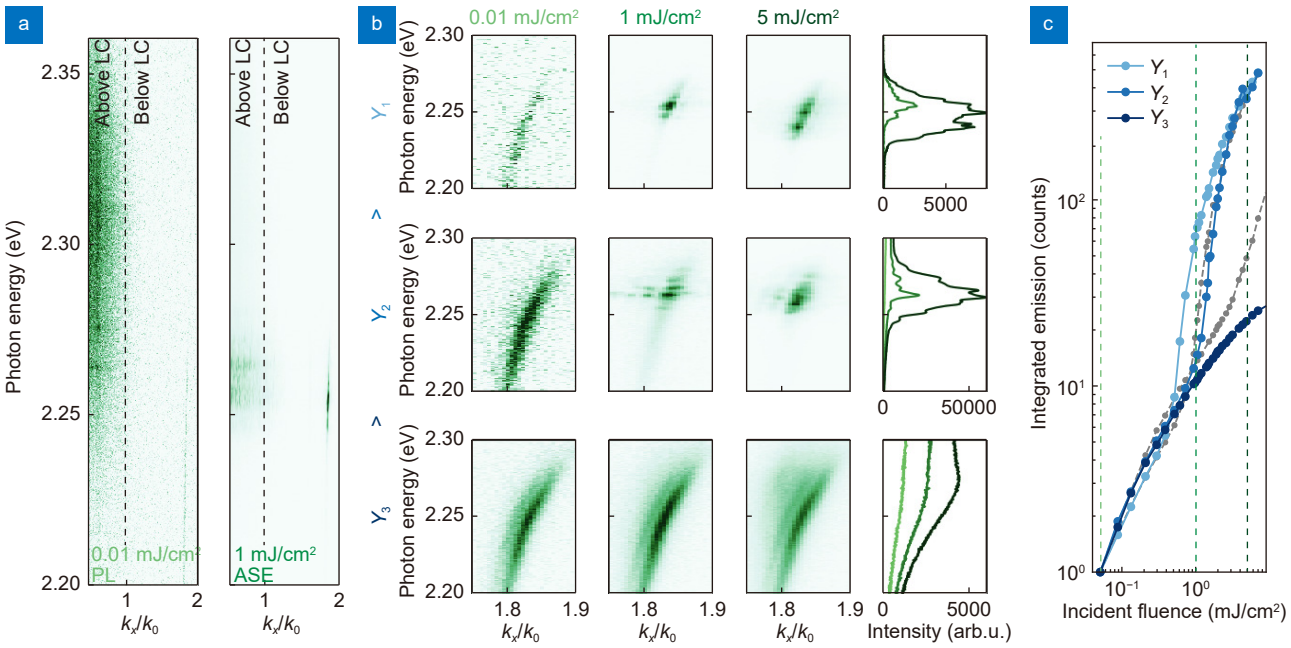

Fig. S1 | (**a**) Angle-resolved emission spectra of guided polariton, obtained at room temperature under femtosecond pump with fluence around 0.01 mJ/cm² and 1 mJ/cm² in the regime of low radiative losses (**b**) Obtained spectra with different pump fluence and SIL distance to the sample. Last dictates mode losses γ. In the figure, the value of the ASE red broadening for high pump fluences decreases with increasing of mode radiative losses. For the highest mode losses ASE was not observed. (**c**) Integrated emission signal as a function of incident fluence for different waveguide mode losses. Colored dots correspond to the optical losses, shown in b, grey dots correspond to the measurements, which are not presented in the text.

leads to the requirement of the higher pump fluence to achieve a nonlinear regime. Eventually, the ASE threshold can be larger than the degradation threshold and we will not be able to see any ASE, as we demonstrate in the case of γ_3 in Fig. S1(c).

Section 2: Interference pattern on angle-resolved emission spectra from perovskite nanowires

Angle-resolved pump-dependent emission measurements from perovskite nanowires are performed in the case of the nanowire axis co-directed with an angle-resolved x-axis. To study the interference pattern we normalized angle-resolved spectra from Fig. 2(g–i) in the main text to the integrated over the k_x/k_0 spectra to make it more pronounced (Fig. S2(a)). At the high pump fluence in the multilasing regime, the emission becomes coherent in the nanowire and outcouples through the edges. The pattern appears due to the interference of the coherent emission from the opposite edges of the nanowire on the BFP (Fig. S2(b)).

The number of the interfered maxima over k_x/k_0 depends on the distance between coherent light sources, or in other words, the physical nanowire length. It should be noticed, that pattern changes the phase over the π with each next order. It can be explained either an even or an odd number of half-length is suited to the nanowire optical length. The parity changes with every next order and therefore the initial phase difference $\Delta\phi_0$ also drops from $\pi + 2\pi n$ to $2\pi n$ or vice versa (Fig. S2(c)). The observed effect helps to distinguish several F-P resonances from each other near the exciton, where it is located very close to each other and when the intensity slightly changes from one resonance to another. By extracting the F-P resonances close to the exciton in the following way, we calculated the free spectral range of the F-P resonances and estimated the group refractive index, shown in Fig. 2(j) in the main text.

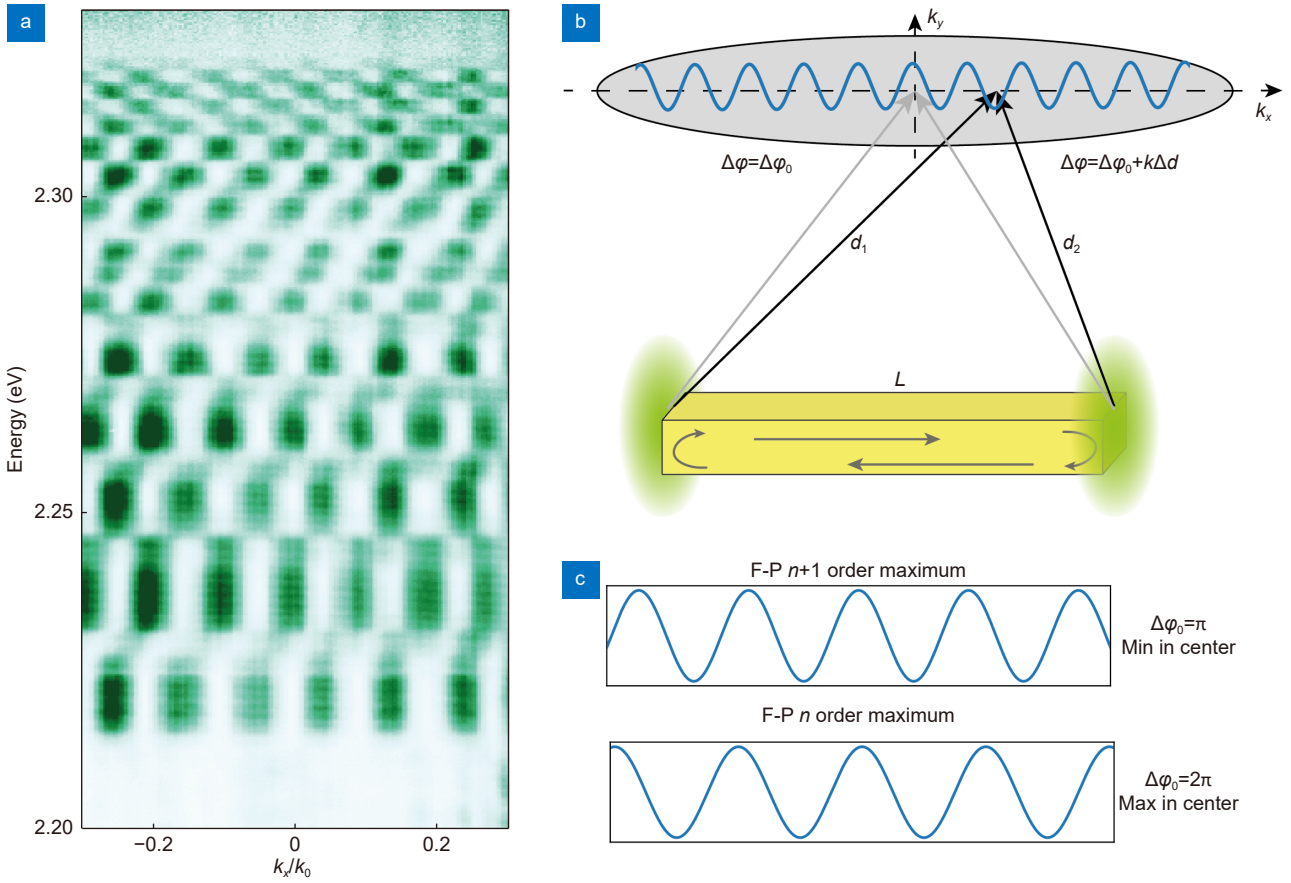

Fig. S2 | (**a**) Angle-resolved emission spectrum, measured at 850 μJ/cm². Data is normalized to the integrated spectrum at each k_x/k_0 to better visualization of the pattern. (**b**) Sketch, visualizing the nature of interference pattern, obtained at panel *a*; (**c**) Visualization of the field distribution in the nanowire of two neighboring F-P resonance. Showed phase difference $\Delta\varphi_0$ is between two different edges of nanowire for both resonances

Section 3: The radiation pattern of Mie-polariton lasing emission from the nanocubes

Pump-dependent emission measurements shown in the main text were done also with angle resolution. Angle-resolved emission spectrum measured from 0.02 μm³ cuboid upon 6 μJ/cm² is shown in Fig. S3(a). It is shown two lasing peaks, noted as "Mode 1" and "Mode 2", which are separated on the wavelength. The third mode ("Mode 3") appears at around 2.3 eV at higher fluence as illustrated in Fig. S3(b), whereas the first two modes become closer to each other and cannot be clearly distinguished. To make it more clear we plotted the section over the wavelength peak centers in the radiation plot demonstrated in Fig. S2(b). Polar plots for modes 1 (orange dots), 2 (green dots), and 3 (blue dots) have different radiation patterns (Fig. S3(c–e)). According to numerical eigenmode analysis "Mode 1" (with $Q_1 \sim 59$) and "Mode2"

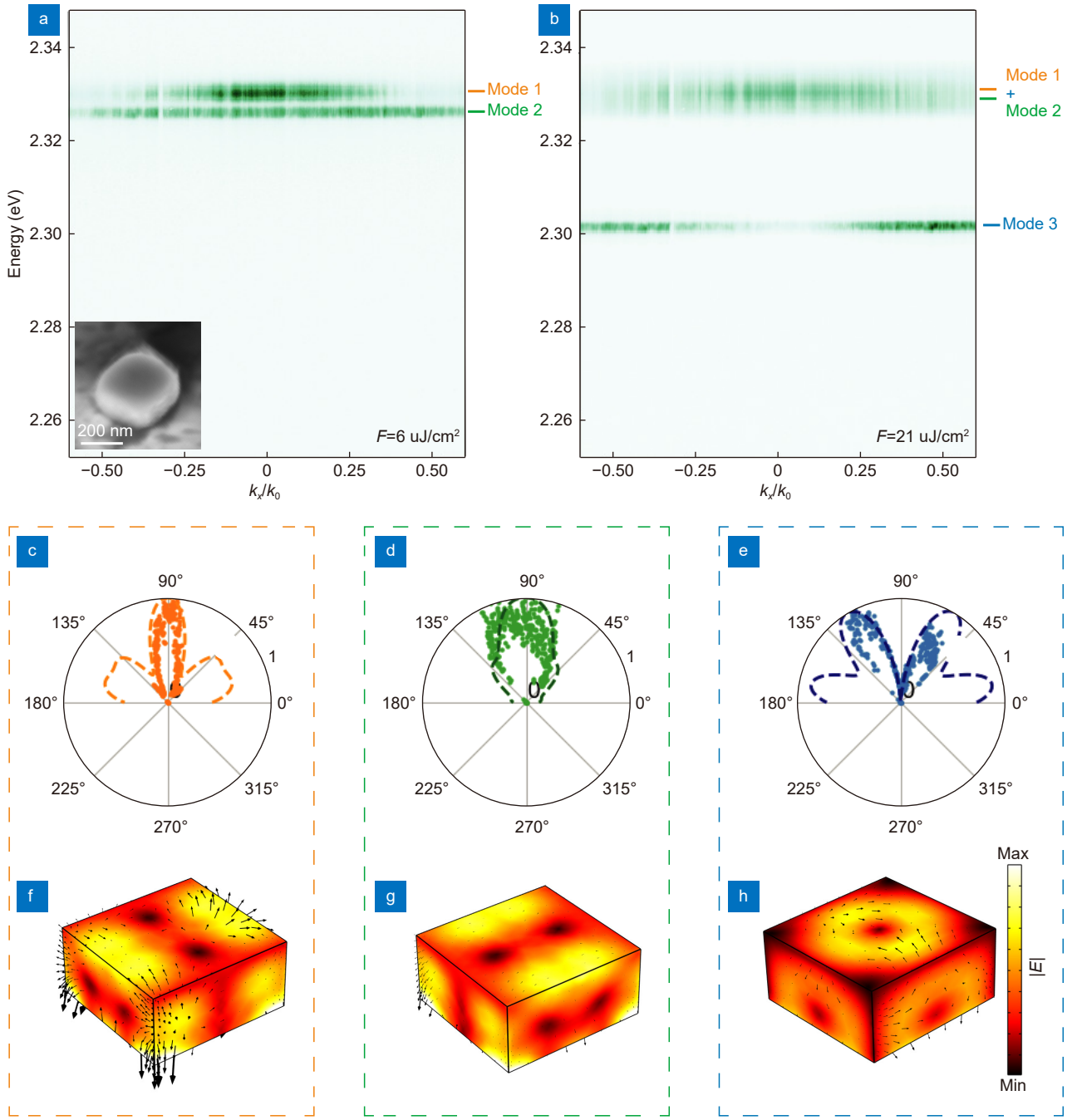

Fig. S3 | (**a**, **b**) Angle-resolved emission spectrum of 0.02 μm³ cuboid upon 6 and 21 μJ/cm² pump fluence. (**c–e**) Radiation distribution of the lasing modes measured experimentally, shown as dots, and simulated far-field pattern, shown as dashed lines. (**f–g**) Corresponding electrical field distribution of the calculated eigenmodes.

($Q_2 \sim 60$) correspond to non-degenerated (because of unequal sides) hybrid mode consisting of mixture of spherical harmonics[S1] involving magnetic octupole with azimuthal number $m = \pm 1$, while the lower energy Mie-mode has $Q_3 \sim 57.8$ with the major contribution from magnetic quadrupole with azimuthal number $m = 2$ (Fig. S3). The spatial electrical field distribution of each eigenmode is presented in Fig. S3(f–h), while calculated far-field directivity is shown in Fig. S3(c–e) by dashed curves matching well the experimental results.

Section 4: Experimental observation of the Mott transition in the perovskite nanocubes

In the previous works, it was suggested, that lasing in the $CsPbBr_3$ nanowires appears above the Mott transition and originated from the electron-hole plasma and plasmonic resonances[S2]. Authors sustained their claim by ultrafast emission spectroscopy, where lasing peaks in the spectra shift to the red region with time, which points to the dependence of the peak position with carrier concentration. However, the same result can be explained by the polariton nature, mentioned in the main text.

To check the lasing origin in our experiments we pump our nanocubes at the highest pump fluences at 6 K to experimentally achieve the Mott transition (Fig. S4(a)). As was already discussed in the main text, we observe a few-lasing peak regimes from the nanocube at the low pump. The quality factor of the lasing mode achieves 1680 (Fig. S4(b)) at 8 μJ/cm². With increasing the pump fluence lasing peaks shift and broad to the blue region. At the fluence around 1000 μJ/cm², broad background PL appears, where stimulated emission still exists. Finally, at fluences above 2500 μJ/cm² lasing stimulated emission disappears and we observe a broad PL spectrum. The spectral center of the broad PL spectrum is shifted from the initial PL center by the value around 32 meV. As the exciton binding energy is estimated to be around 35 meV[S3] we attribute the initial PL to the exciton recombination and PL obtained at the high pump fluence to the band-to-band recombination. In other words, we achieve the Mott transition at the pump fluences around 1000 μJ/cm², which is described in a broad PL background, but the Coulomb correlations between electrons and holes still exist and the polariton lasing can still be maintained but with lower intensity. At the higher fluences, even the correlation disappears with the lasing emission and we obtain clear band-to-band PL. It also should be noted, that according to the experiment, the process is reversible, which means, that we are below the degradation threshold for the particular

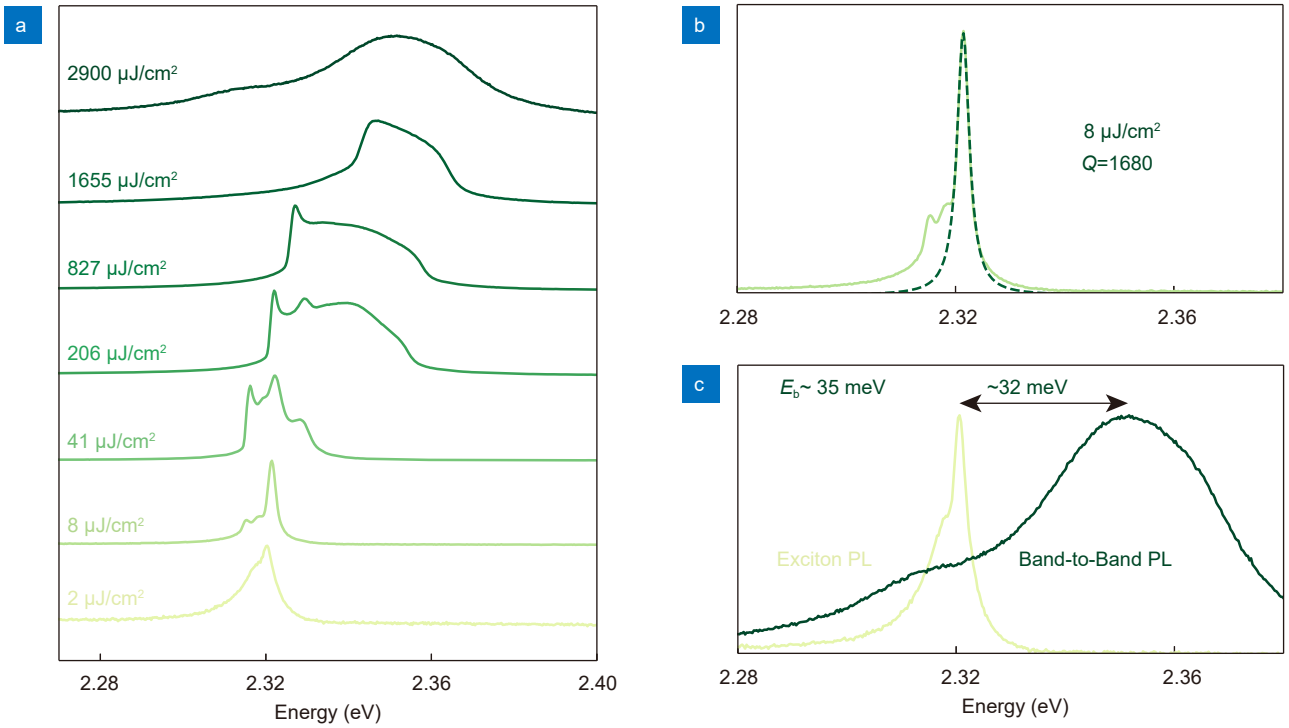

Fig. S4 | (**a**) Integrated emission, obtained under femtosecond pump at 6 K with increasing incident fluence. (**b**) Fit of the lasing peak at 8 μJ/cm² with calculated quality factor. (**c**) Normalized integrated spectra, obtained at 2 and 2900 μJ/cm². TThe first corresponds to exciton PL and the second to band-to-band PL. The difference between these two spectra is close to the exciton binding energy in this material.

perovskite nanocube. According to the estimation, Mott transition fluences are close to the estimated critical Mott concentration, which fits the known experimental data. For more details see Section S5. This data proves, that the lasing emission in our case originated from the exciton-polariton nature of either electron-hole plasma.

Section 5: Estimation of the excited exciton concentration in the nanocubes

In order to compare experimentally achieved Mott transition with literature data we estimate excited carrier concentration in our experiments. In the simplest estimations absorbed optical power intensity can be estimated as

$$I_{\rm abs} = I_{\rm inc} T \left(1 - {\rm e}^{-\kappa k_0 d}\right) \ , \tag{S1}$$

where $I_{\rm inc}$ is incident power, T is transmittance coefficient, κ is the imaginary part of the refractive index at the pump wavelength, k_0 is incident pump $\boldsymbol{k}$-vector and d is the height of the nanocube. In the pulsed pump regime it can be rewritten in the carrier number notations:

$$N_{\rm abs} = N_{\rm inc} T \left(1 - {\rm e}^{-\kappa k_0 d}\right) \ . \tag{S2}$$

The absorbed carrier concentration $n_{\rm abs} = N_{\rm abs}/Sd$, where $\boldsymbol{S}$ is the scale area of the incident pulse. And $N_{\rm inc} = F_{\rm inc}S/E_{\rm ph}$, where $F_{\rm inc}$ is incident fluence and $E_{\rm ph} = hc/\lambda$ is the energy of the single photon at the pump wavelength. The resulting carrier concentration can be estimated as:

$$n_{\rm abs} = T\frac{F_{\rm inc}\left(1 - {\rm e}^{-\kappa k_0 d}\right)}{E_{\rm ph} d} \ . \tag{S3}$$

According to the previous studies, critical exciton Mott transition density is estimated to be equal $n_{\rm M} = 1.0 \times 10^{19}$.[S4] Based on the current approximations in our experiment with a 490 nm pulsed pump, such concentrations are reachable at the fluences around 300 μJ/cm^2. Deviations from the experimental observation can be explained by overestimation of the excited exciton concentration, which appeared from overestimated absorption coefficient at 6 K, Gaussian distribution of the pump spot profile, and optical effects due to the substrate, and nanocube faces. Also, it should be noted, that estimated Mott concentration does not take into account polaron effects in the material[S5], which increases critical Mott concentration[S6]. Nevertheless, the order of the estimated excited exciton concentration and Mott concentration is well agreed with experimental observations and prove, that observed lasing and ASE regimes originated from exciton-polariton nature.

Section 6: Optical properties of $CsPbBr_3$ cuboids at room temperature

Obtained nanocuboids suspension in hexane reveals bright green emission peaked at λ_c 524 nm with FWHM ~ 21 nm upon UV lamp excitation, while extinction spectrum contains a sharp dip in the region of PL maximum (Fig. S5(a)). This dip is attributed to Fano resonance[S7]. Notably, the suspension consists of nanocuboids of various hydrodynamic sizes from around 200 to 1000 nm which are slightly overestimated based on DLS measurements as compared to the real sizes (Fig. S5(b)). According to the collected data the majority of nanocuboids have hydrodynamic diameter of about 296 nm. A suspension of perovskite cuboids was drop-casted on a metal-dielectric substrate (Fig. S6(a–b)). Regular shape and smooth facets of cavities with various dimensions were confirmed by SEM (Fig. S7(a–d)). Scattering from single resonators was studied by means of dark-field spectroscopy at room temperature. Scattering spectra were measured by optical microscope (Carl Zeiss Axio Imager.A2m). The sample was illuminated in dark-field mode by a broadband halogen lamp (HAL 100) via 100x objective (EC Epiplan-NEOFLUAR). The scattered signal from single cuboid was collected by the same objective and sent to the spectrometer (Ocean Optics) through 100-μm optical fiber. The spectra showed sharp resonances of Mie-type which spectral position and order depends on cavity size. Therefore, small cuboids with size around 200 nm possesses pronounced magnetic dipole and quadrupole Mie-resonances. Increase in cavity size causes shift to low-energy of first-order resonances (purple dashed line) along with appearance of new high-order resonances near the exciton energy (green dashed line) (Fig. S7(e)). Notably, the resultant scattering spectrum is a superposition of resonator's Mie modes which allows to estimate the approximate geometrical parameters of cuboids.

To solve the inverse scattering problem we applied a relevant numerical model based on the T-matrix method and the freely available software "Smuthi"[S8–S12]. "Smuthi" is a Python package for modeling electromagnetic scattering by

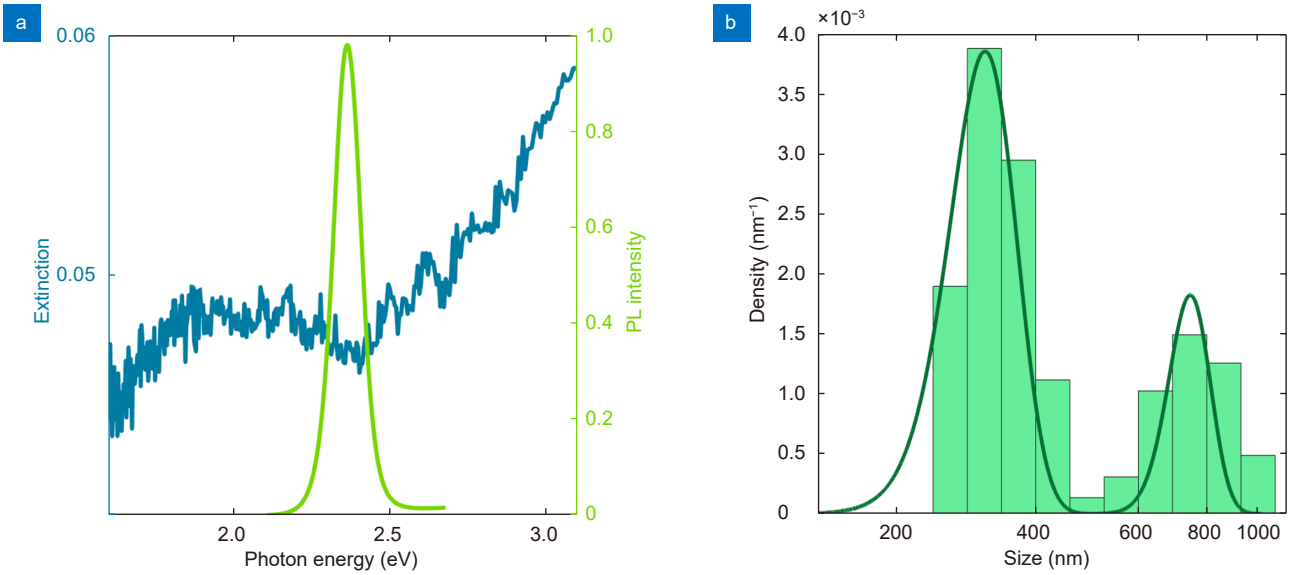

Fig. S5 | (**a**) Photoluminescense and extinction spectra of nanocuboids suspension in n-hexane. (**b**) Size distribution histogram of nanocuboids suspension in n-hexane.

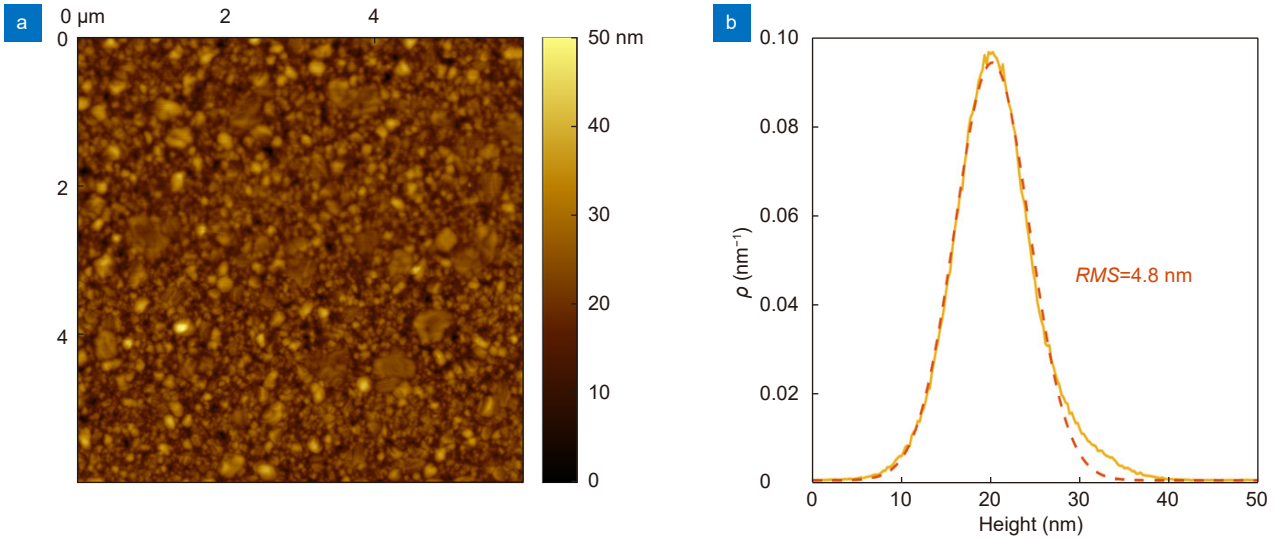

Fig. S6 | (**a**) AFM picture of the obtained metal-dielectric Al_2O_3/Ag/Si substrate morphology with width of thin Ag film of 50 nm. (**b**) Histogram of the film height extracted from the AFM measurement. Fitted Gaussian distribution gives standard deviation equal to 4.8 nm.

one or more wavelength scale objects in layered systems efficiently and accurately. The software integrates the T-matrix method of single-particle scattering with the scattering matrix formalism for electromagnetic field propagation through planar interfaces. This method was used to find optimal multilayer systems designs and to obtain an extinction cross-section decomposition for all multipole components (in our case only for the dipole components). To estimate the T-matrices of nonspherical particles, "Smuthi" uses the advanced NFM-DS ("Null-field Method with Discrete Sources") FORTRAN[S13] software. T-matrices computed with NFM-DS are processed in the "Smuthi" software to solve the problem of multiple scattering between such particles as well as between particles and layered media.

As described earlier in the main text, metal-dielectric substrates are widely used to enhance field localization efficiency and mode selectivity[S14,S15]. To demonstrate the promising potential of plasmonic substrates, we numerically simulate the scattering behavior of $CsPbBr_3$ nanocuboids on Al_2O_3/Ag/Si substrates (bottom row in Fig. S8) and compare with similar nanocuboids on glass substrates (top row in Fig. S8).

We evaluated a comparison of scattering spectra for a broad range of cube sizes (Fig. S8(a, d), revealing an order of magnitude higher scattering efficiency on the Al_2O_3/Ag/Si substrate, as well as a mode contrast. To validate the T-matrix method, the experimental scattering spectra obtained for similar $CsPbBr_3$ nanocuboids on the glass and Al_2O_3/Ag/Si

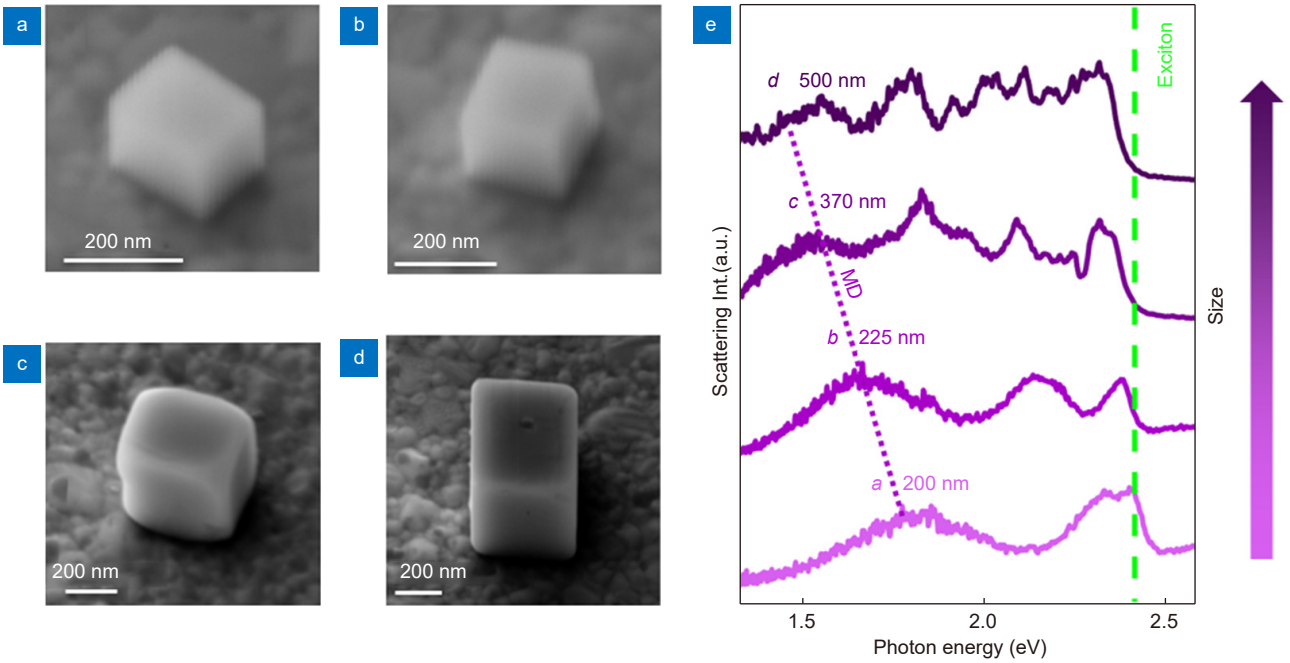

Fig. S7 | (**a**–**d**) SEM images of $CsPbBr_3$ cuboids with various characteristic sizes (*a*: 200 nm; *b*: 225 nm; *c*: 370 nm; *d*: 500 nm) and (**e**) corresponding scattering spectra at room temperature. Green dashed line corresponds to exciton energy and purple dashed line to shift of magnetic dipole resonance.

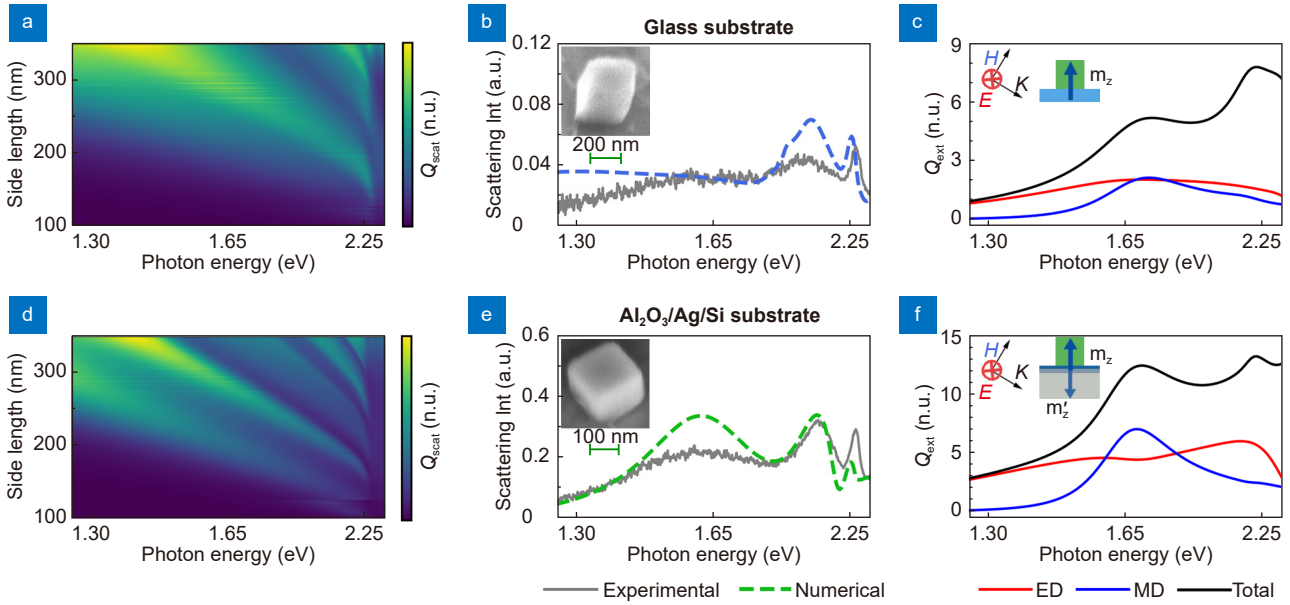

Fig. S8 | Comparison of scattering properties of $CsPbBr_3$ cuboids on a glass (upper row) and on a metal-dielectric (bottom row) substrates. Scattering efficiency Q_{scat} for $CsPbBr_3$ nanocubes with different sizes on a glass substrate (**a**) and on a Al_2O_3/Ag/Si substrate (**d**). Comparison of experimental (solid line) and numerical (dashed line) results of scattering spectra for the nanocuboid (320x370x260~nm^3) on a glass substrate (**b**) and the nanocuboid (205×225×195~nm^3) on a Al_2O_3/Ag/Si substrate (**e**). Insets: SEM images of corresponding nanocuboids. Electric (red curve) and magnetic (blue curve) dipole contributions in extinction efficiency Q_{ext} (black curve corresponds to total extinction) for 242~nm cube on a glass substrate (**c**) and on a Al_2O_3/Ag/Si substrate (**f**), respectively. Insets: schematic representation of incident wave and formation of the image dipole moment.

substrates were compared with those predicted theoretically. As shown in Fig. S8(b, e), obtained results demonstrate an excellent agreement between the numerical and experimental data, where the difference in amplitude for the resonance at high energy can be explained by the large absorption in this range. Notably, the scattering spectra were simulated for systems similar to the experimental ones, taking into account all input parameters of the experimental conditions in-

cluding geometrical parameters (the difference in width, length and height). Improved scattering efficiency and selectivity of modes on plasmonic substrates is related to the formation of mirror-image Mie modes[S14,S15]. The multipole decomposition of extinction cross-section of a 242 nm $CsPbBr_3$ cube excited in TE mode is shown in (Fig. S8(c, f). TE polarization of the incoming light leads to the efficient excitation of the z-oriented magnetic dipole and, in case of plasmonic substrate, formation of a magnetic dipole-image with anti-phase (inset in Fig. S8(f)). The interaction of anti-phase dipole sources leads to an increase in the intensity and Q-factor of magnetic dipole component in decomposition of the extinction cross-section for a cube on metal-dielectric substrate compared to the same cube on glass.

Therefore, the integration of compact semiconductor resonators with metal-dielectric substrates is highly promising for lasing application. Moreover, the developed approach is highly useful for fast detection and primary characterization of nanocuboids, promising for lasing study, allowing to avoid premature SEM measurements, which destroys optical properties via increasing nonradiative traps.

Section 7: Calculation of cold dispersion

Analytical dispersion of $CsPbBr_3$ at room and 6 K temperatures have been obtained from measurements of reflection coefficient of $CsPbBr_3$ microplates (MPs) by using of transfer matrix method (TMM).

$CsPbBr_3$ MPs with various thicknesses (from 145 nm up to 1485 nm) were obtained on glass substrate according to the procedure reported by Zhizhchenko et al.[S16] (Fig. S9(a)). Reflection spectra were measured from 18 MPs at room and cryogenic temperatures upon broadband halogen lamp excitation at almost normal incidence. Reflected signal was collected from the center of MP through 100 μm-pinhole to avoid scattering from edges. The collected spectra were normalized to the incoming spectrum of source. Resulting experimental dependencies of reflection coefficient on photon energy obtained for selected five MPs with different thicknesses at room and cryogenic temperatures are shown in Fig. S9(b, c) .

To obtain the refractive index and the extinction coefficient of the perovskite MP on a glass substrate TMM has been employed. By treating the substrate as a semi-infinite space, the following analytical formula for the reflection coefficient can be derived:

$$R_t^{(\mathrm{TMM})}(\lambda,T)=\left|\frac{\left(1-\frac{n_{\mathrm{plate}}(\lambda,T)}{n_0}\right)\left(1+\frac{n_{\mathrm{s}}}{n_{\mathrm{plate}}(\lambda,T)}\right)\mathrm{e}^{-\mathrm{i}k_z t}+\left(1+\frac{n_{\mathrm{plate}}(\lambda,T)}{n_0}\right)\left(1-\frac{n_{\mathrm{s}}}{n_{\mathrm{plate}}(\lambda,T)}\right)\mathrm{e}^{\mathrm{i}k_z t}}{\left(1+\frac{n_{\mathrm{plate}}(\lambda,T)}{n_0}\right)\left(1+\frac{n_{\mathrm{s}}}{n_{\mathrm{plate}}(\lambda,T)}\right)\mathrm{e}^{-\mathrm{i}k_z t}+\left(1-\frac{n_{\mathrm{plate}}(\lambda,T)}{n_0}\right)\left(1-\frac{n_{\mathrm{s}}}{n_{\mathrm{plate}}(\lambda,T)}\right)\mathrm{e}^{\mathrm{i}k_z t}}\right|^2, \tag{S4}$$

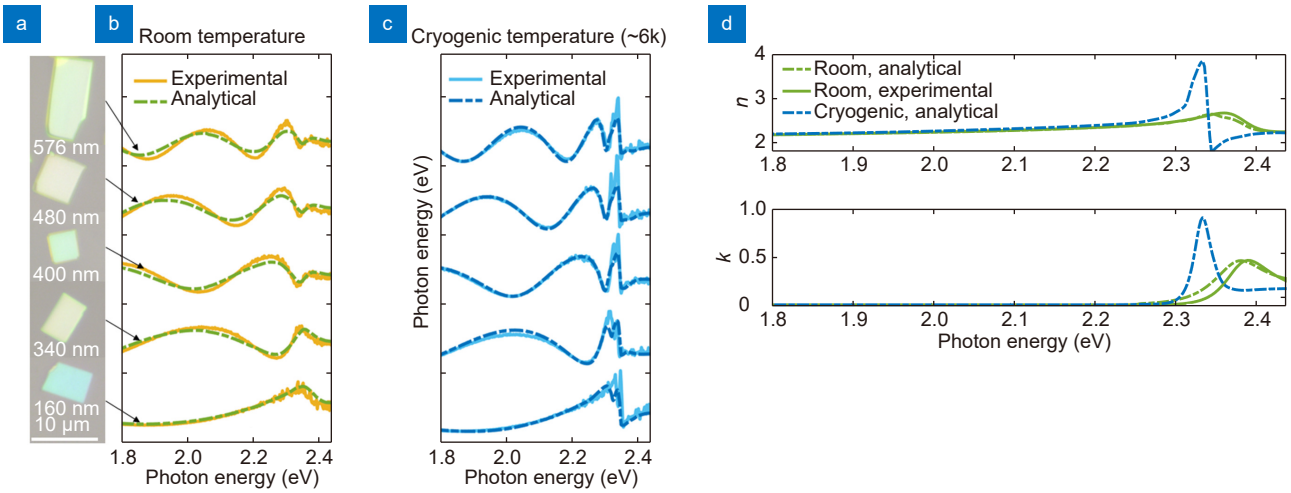

Fig. S9 | (**a**) Brightfield images of $CsPbBr_3$ plates with various thickness: 160 nm, 340 nm, 400 nm, 480 nm and 576 nm. Scale bar equals to 10 μm. (**b**) Experimental (continuous) and analytical (dashed) reflection spectra of $CsPbBr_3$ plates with various thickness from (a) at room temperature. (**c**) Experimental (continuous) and analytical (dashed) reflection spectra of $CsPbBr_3$ plates with various thickness from (a) at cryogenic (~6 K) temperature. (**d**) Real and imaginary part of $CsPbBr_3$ refractive index obtained from analytical calculation at room and cryogenic (~6 K) temperatures (dashed green and blue curve, respectively), whereas the experimental data at room temperature is taken from work[S17] (solid green curve).

where $R^{(\mathrm{TMM})}(\lambda, T)$ is the intensity reflection coefficient depending on the wavelength and temperature, t is the thickness of perovskite MP, $n_{\mathrm{plate}}(\lambda, T)$ is the complex refractive index of perovskite MP, n_0 is the refractive index of the surrounding atmosphere (we consider $n_0 = 1$), n_s is the substrate refractive index (we consider $n_s = 1.55$), and

$$k_z = \frac{2\pi}{\lambda}\sqrt{n_{\mathrm{film}}^2(\lambda, T) - n_0^2 \sin^2(\theta)}\ , \tag{S5}$$

where θ is the incidence angle (we consider $\theta = 0$).

In order to parametrize the dispersion, we define the function $n_{\mathrm{plate}}(\lambda)$ by its values at fixed wavelengths and use shape-preserving piecewise cubic interpolation to interconnect these points. Namely, we fix the refractive index at 20 uniformly distributed wavelengths in the 500 nm $\leq \lambda <$ 550 nm range, and the refractive index at 5 uniformly distributed points in the 550 nm $\leq \lambda \leq$ 750 nm range. The extinction coefficient is taken from direct measurements. Therefore we obtain a complex function $n_{\mathrm{plate}}(\lambda, T)$ dependent on 24 fitting parameters (for a single temperature).

Additionally, due to the experimental errors, we introduce the following fitting parameters. First, due to the MP's surface corrugations, the measurement of the plate thicknesses with a profilometer has an experimental error of ±30 nm, so we introduce the thickness correction Δt_i for each plate, which is varied between −30 nm and +30 nm. Second, due to the experimental errors in the reflection measurement, the reflection spectra were multiplied by the correction coefficients K_i (for room temperature) and K_i' (for 6 K), which became fitting parameters. The typical values of the correction coefficients lie between 0.9 and 1.1. The spectra are fitted together by minimizing the function F by varying the total 102 fitting parameters:

$$F = \sum_{i,j} \left| K_i R_{t_i}^{(\mathrm{exp})}(\lambda_j, 250\ \mathrm{K}) - R_{t_i+\Delta t_i}^{(\mathrm{TMM})}(\lambda_j, 250\ \mathrm{K}) \right|^2 + \left| K_i' R_{t_i}^{(\mathrm{exp})}(\lambda_j, 6\ \mathrm{K}) - R_{t_i+\Delta t_i}^{(\mathrm{TMM})}(\lambda_j, 6\ \mathrm{K}) \right|^2\ , \tag{S6}$$

where $R^{(\mathrm{exp})}$ is the reflection coefficient measured experimentally.

The resulting reflection spectra are shown in Fig. S9(b, c) labelled as "analytical". The dispersions of MPs at room temperature and 6 K obtained by the fitting procedure described above are shown in Fig. S9(d). Notably, the dispersion obtained at room temperature is in a good agreement with one obtained experimentally for the same crystalline $CsPbBr_3$ material[S17].

Section 8: Photoluminescence decay measurements

To obtain lasing in perovskite cavities with physical volume less than 0.02 μm^3 they were integrated with metal-dielectric substrate which selectively enhances localization of Mie-resonances in nanocuboids due to a mirror-image

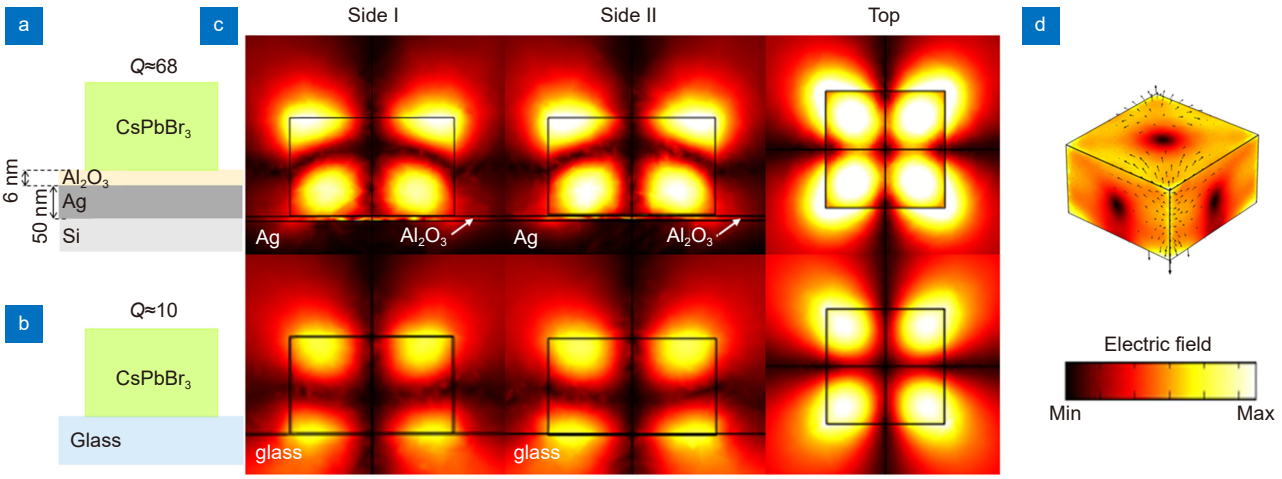

Fig. S10 | Effect of plasmonic substrate on EQ mode localization in 0.007 μm^3 cuboid. Schematic images of $CsPbBr_3$ cuboid with the same size placed on metal-dielectric (**a**) and glass (**b**) substrates. (**c**) Normal electric field distribution in three different cross-sections (side I, side II, and top), where the upper row corresponds to cuboid on a plasmonic substrate (a), while the bottom one to glass (b). (**d**) Electric field distribution for the mode over the surface of the cuboid, where dominating contribution comes from EQ mode with azimuthal number m=2.

effect[S14,S15,S18]. This enhancement related to Purcell effect and can be defined by Purcell factor F_P proportional to $\frac{Q}{V_c}$ value and expressed as follows: $F_P = \frac{3}{4\pi^2}\frac{\lambda^3}{V_c}Q$, where λ is a wavelength inside cavity, Q and V_c are quality factor and volume of mode, respectively. Experimentally, Purcell effect can be observed by shortening of the decay (lifetime) of spontaneous emission: $F_P = \gamma_R/\gamma$, where γ_R and γ – are radiative decay rates of dipole source in cavity or bulk, respectively. Therefore, PL decay in single cuboids with similar size on glass and plasmonic substrates (Fig. S11(a, b)) was studied in the same excitation conditions (pump fluence around 0.1 μJcm^{-2}, pulse duration around 220 fs, repetition rate equaled to 100 kHz and pump wavelength is centred to 490 nm) at room and cryogenic temperatures. At room temperature, PL lifetime equals to τ_{gl} = 1.9 ns and τ_{pl} = 0.5 ns for nanocuboids on glass and metal-dielectric substrates, respectively (Fig. S11(c, d)). At cryogenic temperature, lifetimes are getting nearly 3 times shorter for the glass substrate and at least more than 5 times shorter for plasmonic one that cannot be precisely resolved because of instrumental response (black curve in Fig. S11(b-c)) of the detector. Thus, the positive influence of metal-dielectric substrate on optical properties of perovskite nanocuboids was confirmed by time-resolved measurements.

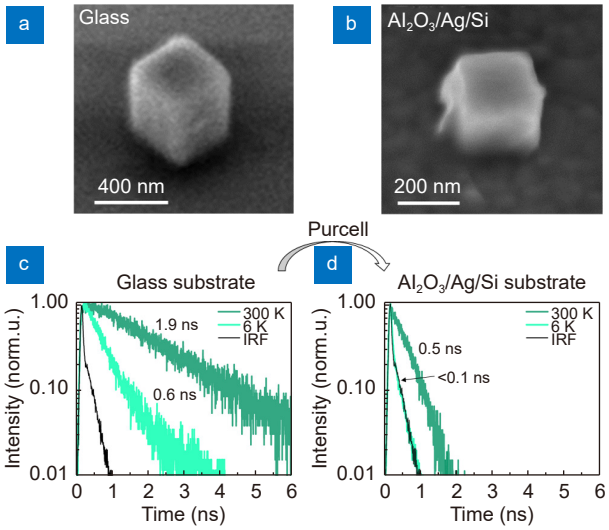

Fig. S11 | (**a**, **b**) SEM images of $CsPbBr_3$ nanocuboids on plasmonic and glass substrates, respectively. (**c**, **d**) Photoluminescence decay curves of $CsPbBr_3$ nanocuboids on plasmonic and glass substrates, respectively, obtained at room (300 K) and cryogenic (6 K) temperatures. Black decay corresponds to IRF.

Table S1 | Comparison table of nanolasers for the last 12 years. This work is highlighted by the bold font. In the table *L* - length, *D* - diameter, *H* - height, *W* - width, * - this work.

	Type	Active media	Cavity Size	V (μm^3)	V/λ^3	Pump	Threshold	Temp.	Ref	Year
UV	Wire	GaN 375 nm	*L*:15 μm *D*: 130 nm	0.1	2.08	100 kHz 10 ns	35 mJ/cm²	RT	ref.[S19]	2014
	Wire	ZnO 370 nm	*L*: 1.24 μm *H*=*W*: 28 nm	0.003	0.05	1 kHz 0.5 ns	30 mJ/cm²	77 K	ref.[S20]	2015
	Wire	ZnO 380 nm	*L*: 1.7 μm *H*=*W*: 30 nm	0.004	0.072	1 kHz 0.5 ns	55 mJ/cm²	RT	ref.[S21]	2016
	Wire	ZnO 370 nm	*L*: 1.5 μm *H*=*W*: 30 nm	0.004	0.069	1 kHz 0.5 ns	27 mJ/cm²	77 K	ref.[S22]	2018
	Wire	ZnO 372 nm	*L*: 0.9 μm *H*=*W*: 35 nm	0.003	0.06	1 kHz 0.5 ns	45 mJ/cm²	77 K	ref.[S23]	2018
VIS	Bundle of rods	InGaN/GaN 533 nm	*L*: 680 nm *H*=*W*: 530 nm	0.13	0.44	90 MHz 150 fs	3 mJ/cm²	7 K	ref.[S24]	2011
	Wire	$MAPbI_3$ 780 nm	*L*: 7.5 μm *H*: 600 nm *W*: 300 nm	1.35	2.84	250 kHz 150 fs	0.4 μJ/cm²	RT	ref.[S25]	2015
	Square plate	$MAPbBr_3$ 557 nm	*L*=*W*: 2 μm *H*: 0.6 μm	2.4	13.89	1 kHz 120 fs	3.6 μJ/cm²	RT	ref.[S26]	2015
	Wire	$MAPbI_3$ 768 nm	*L*: 5.1 μm *H*: 126 *W*: 167 nm	0.1	0.24	1 kHz 120 fs	29 μJ/cm²	RT	ref.[S27]	2016
	Sphere	$CsPbBr_3$ 545.2 nm	*D*: 780 nm	0.48	2.95	10 kHz 40 fs	0.42 μJ/cm²	RT	ref.[S28]	2017
	Square plate	CdSe 700 nm	*H*: 137 nm *L*=*W*: 1 μm	0.14	0.4	1 kHz 4.5 ns	45 mJ/cm²	RT	ref.[S29]	2017
	Hex. plate	$MAPbI_3$ 770 nm	*H*: 50 nm *L*: 10 μm	13	28.5	1 kHz 100 fs	59.2 μJ/cm²	RT	ref.[S30]	2018
	Cuboid	$CsPbBr_3$ 540 nm	*W*=*L*=*H*: 400 nm	0.064	0.49	1 kHz 35 fs	40.2 μJ/cm²	RT	ref.[S31]	2018
	Wire	$CsPbBr_3$ 524 nm	*W*=*H*: 250 nm *L*: 2 μm	0.125	0.9	CW	46 mW/cm²	4K	ref.[S32]	2018
	Wire	$CsPbBr_3$ 534 nm	*L*: 3.5 μm *H*: 120 nm *W*: 200 nm	0.084	0.55	1 kHz 100 fs	12 μJ/cm²	RT	ref.[S33]	2018
	Cuboid	$CsPbBr_3$ 533 nm	*W*=*L*=*H*: 310 nm	0.03	0.197	100 kHz 150fs	300 μJ/cm²	RT	ref.[S34]	2020
	Cuboid	$CsPbBr_3$ 540 nm	*W*: 580 nm *L*: 560 nm *H*: 320 nm	0.1	0.66	20 kHz 4 ns	0.48 mJ/cm²	RT	ref.[S35]	2021
	Wire	$CsPbBr_3$ 534 nm	*L*: 4.5 μm *W*: 260 nm *H*: 290 nm	0.34	2.23	50 kHz 150 fs	24 μJ/cm²	RT	ref.[S36]	2022
	Cuboid	**$CsPbBr_3$ 533 nm**	***W*: 215 nm *L*: 225 nm *H*: 140 nm**	**0.007**	**0.04**	**100 kHz 220 fs**	**1 μJ/cm²**	**6.4 K**	*	**2023**
NIR	Plasm. disk	InGaAsP 1430 nm	*D*: 920 nm *H*: 1.28 μm	0.2	0.07	300 kHz 12 ns	1 mJ/cm²	RT	ref.[S37]	2010
	Plasm. cylinder	InGaAsP 1400 nm	*D*: 400 nm *H*: 210 nm	0.03	0.01	CW	Thresholdless	4.5 K	ref.[S38]	2012
	Cylinder	GaAs 825 nm	*D*: 500 nm *H*: 330 nm	0.07	0.1	20 kHz 200 fs	260 μJ/cm²	77 K	ref.[S39]	2020
	Disk	WS_2 868.5 nm	*D*: 3 μm *H*: 50 nm	0.35	0.58	CW	1.25 kW/cm²	RT	ref.[S40]	2022

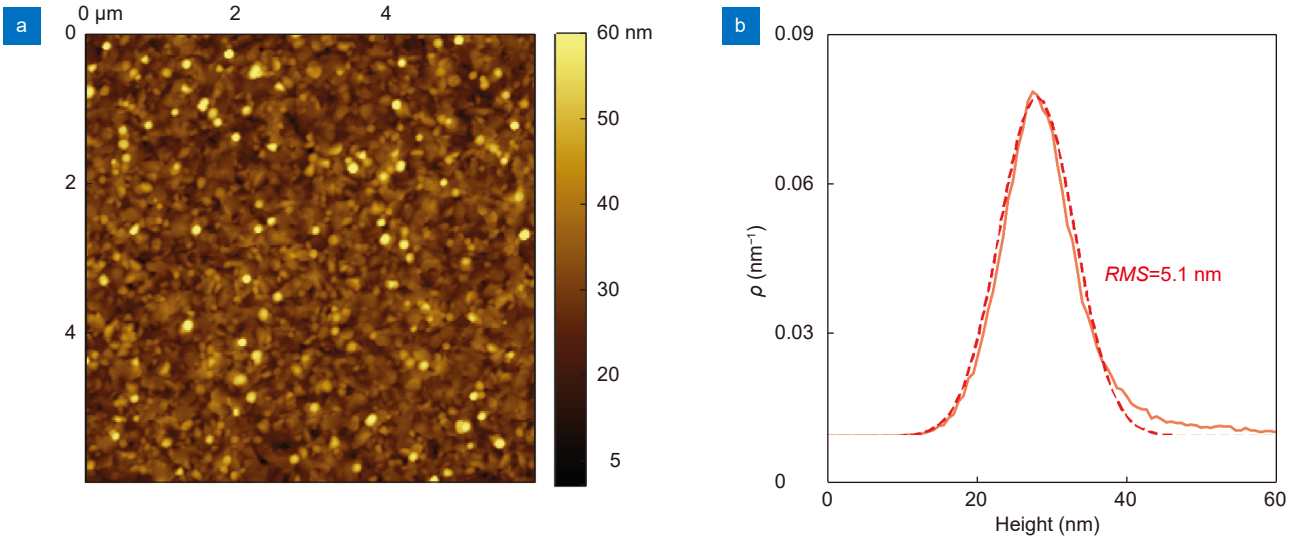

Fig. S12 | (**a**) AFM picture of the studied lead-bromide perovskite thin film morphology with width of 120 nm. (**b**) Histogram of the film height extracted from the AFM measurement. Fitted Gaussian distribution gives standard deviation equal to 5.1 nm.

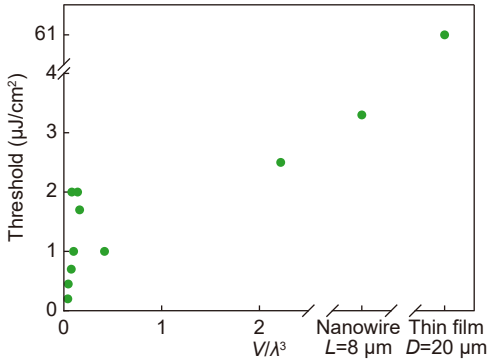

Fig. S13 | Stimulated emission pump fluence threshold of studied perovskite structures at 6 K depending on the size. For nanocubes size normalized on emission wavelength V/λ^3 is shown. Threshold of multilasing in nanowire was determined, L is the length of studied nanowire with lateral cross section around 600 nm. Threshold of studied perovsite thin film with width of 100 nm was determined, diameter of pumping spot D is equal to 20 μm.

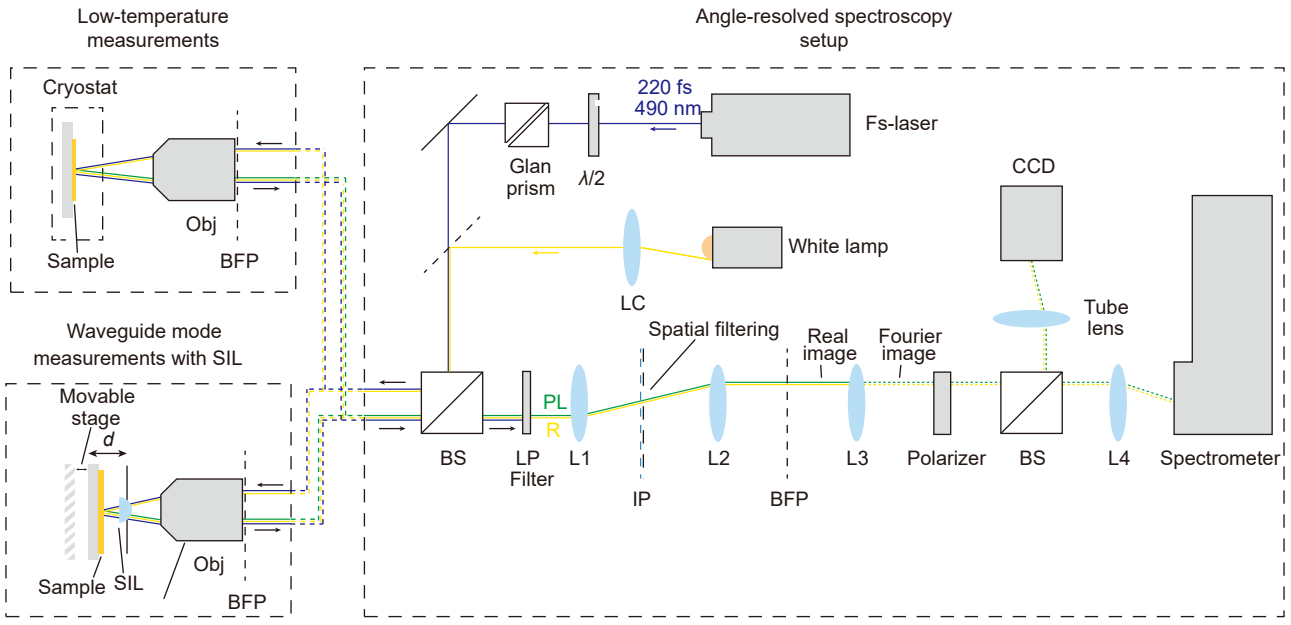

Fig. S14 | Scheme of the optical experimental setup.

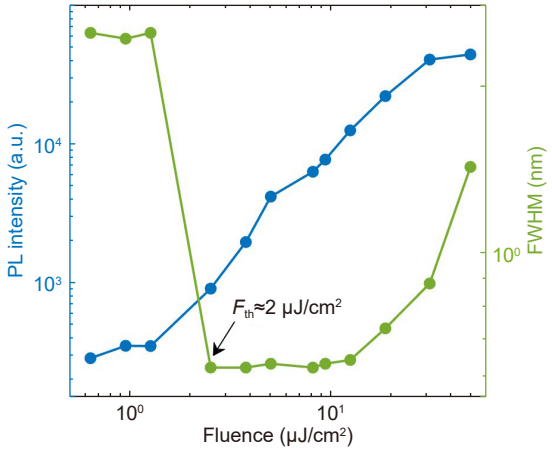

Fig. S15 | PL intensity and FWHM value versus fluence for the nanolaser in Fig. 3(c) of the main text

References

S1. Gladyshev S, Frizyuk K, Bogdanov A. Symmetry analysis and multipole classification of eigenmodes in electromagnetic resonators for engineering their optical properties. *Phys Rev B* **102**, 075103 (2020).

S2. Schlaus AP, Spencer MS, Miyata K et al. How lasing happens in $CsPbBr_3$ perovskite nanowires. *Nat Commun* **10**, 265 (2019).

S3. Khmelevskaia D, Markina D, Tonkaev P et al. Excitonic versus free-carrier contributions to the nonlinearly excited photoluminescence in $CsPbBr_3$ perovskites. *ACS Photonics* **9**, 179–189 (2022).

S4. Su R, Fieramosca A, Zhang Q et al. Perovskite semiconductors for room-temperature exciton-polaritonics. *Nat Mater* **20**, 1315–1324 (2021).

S5. Evans TJS, Miyata K, Joshi PP et al. Competition between hot-electron cooling and large polaron screening in $CsPbBr_3$ perovskite single crystals. *J Phys Chem C* **122**, 13724–13730 (2018).

S6. Masharin M, Masharin VA, Masharin FA et al. Polaron-enhanced polariton nonlinearity in lead halide perovskites. *Nano Lett* **22**, 9092–9099 (2022).

S7. Tiguntseva EY, Baranov DG, Pushkarev AP et al. Tunable hybrid fano resonances in halide perovskite nanoparticles. *Nano Lett* **18**, 5522–5529 (2018).

S8. Egel A, Lemmer U. Dipole emission in stratified media with multiple spherical scatterers: Enhanced outcoupling from oleds. *J Quant Spectrosc Radiat Transf* **148**, 165–176 (2014).

S9. Egel A, Kettlitz SW, Lemmer U. Efficient evaluation of sommerfeld integrals for the optical simulation of many scattering particles in planarly layered media. *J Opt Soc Am A* **33**, 698–706 (2016).

S10. Egel A, Gomard G, Kettlitz SW et al. Accurate optical simulation of nano-particle based internal scattering layers for light outcoupling from organic light emitting diodes. *J Opt* **19**, 025605 (2017).

S11. Theobald D, Egel A, Gomard G et al. Plane-wave coupling formalism for *T*-matrix simulations of light scattering by nonspherical particles. *Phys Rev A* **96**, 033822 (2017).

S12. Egel A, Czajkowski KM, Theobald D et al. SMUTHI: a python package for the simulation of light scattering by multiple particles near or between planar interfaces. *J Quant Spectrosc Radiat Transf* **273**, 107846 (2021).

S13. Doicu A, Wriedt T, Eremin YA. *Light Scattering by Systems of Particles: Null-Field Method with Discrete Sources: Theory and Programs* (Springer, Berlin, 2006).

S14. Xifré-Pérez E, Shi L, Tuzer U et al. Mirror-image-induced magnetic modes. *ACS Nano* **7**, 664–668 (2013).

S15. Sinev I, Iorsh I, Bogdanov A et al. Polarization control over electric and magnetic dipole resonances of dielectric nanoparticles on metallic films. *Laser Photonics Rev* **10**, 799–806 (2016).

S16. Zhizhchenko AY, Cherepakhin AB, Masharin MA et al. Direct imprinting of laser field on halide perovskite single crystal for advanced photonic applications. *Laser Photonics Rev* **15**, 2100094 (2021).

S17. Ermolaev G, Pushkarev AP, Zhizhchenko A et al. Giant and tunable excitonic optical anisotropy in single-crystal halide perovskites. *Nano Lett* **23**, 2570–2577 (2023).

S18. Markovich DL, Ginzburg P, Samusev A et al. Magnetic dipole radiation tailored by substrates: numerical investigation. *Opt Express* **22**, 10693–10702 (2014).

S19. Zhang Q, Li GY, Liu XF et al. A room temperature low-threshold ultraviolet plasmonic nanolaser. *Nat Commun* **5**, 4953 (2014).

S20. Chou YH, Chou BT, Chiang CK et al. Ultrastrong mode confinement in zno surface plasmon nanolasers. *ACS Nano* **9**, 3978–3983 (2015).

S21. Chou YH, Wu YM, Hong KB et al. High-operation-temperature plasmonic nanolasers on single-crystalline aluminum. *Nano Lett* **16**, 3179–3186 (2016).

S22. Chou YH, Hong KB, Chang CT et al. Ultracompact pseudowedge plasmonic lasers and laser arrays. *Nano Lett* **18**, 747–753 (2018).

S23. Cheng PJ, Huang ZT, Li JH et al. High-performance plasmonic nanolasers with a nanotrench defect cavity for sensing applications. *ACS Photonics* **5**, 2638–2644 (2018).

S24. Wu CY, Kuo CT, Wang CY et al. Plasmonic green nanolaser based on a metal–oxide–semiconductor structure. *Nano Lett* **11**, 4256–4260 (2011).
S25. Zhu HM, Fu YP, Meng F et al. Lead halide perovskite nanowire lasers with low lasing thresholds and high quality factors. *Nat Mater* **14**, 636–642 (2015).
S26. Liao Q, Hu K, Zhang HH et al. Perovskite microdisk microlasers self-assembled from solution. *Adv Mater* **27**, 3405–3410 (2015).
S27. Yu HC, Ren KK, Wu Q et al. Organic–inorganic perovskite plasmonic nanowire lasers with a low threshold and a good thermal stability. *Nanoscale* **8**, 19536–19540 (2016).
S28. Tang B, Dong HX, Sun LX et al. Single-mode lasers based on cesium lead halide perovskite submicron spheres. *ACS Nano* **11**, 10681–10688 (2017).
S29. Wang S, Wang XY, Li B et al. Unusual scaling laws for plasmonic nanolasers beyond the diffraction limit. *Nat Commun* **8**, 1889 (2017).
S30. Huang C, Sun WZ, Fan YB et al. Formation of lead halide perovskite based plasmonic nanolasers and nanolaser arrays by tailoring the substrate. *ACS Nano* **12**, 3865–3874 (2018).
S31. Liu ZZ, Yang J, Du J et al. Robust subwavelength single-mode perovskite nanocuboid laser. *ACS Nano* **12**, 5923–5931 (2018).
S32. Jiang L, Liu RM, Su RL et al. Continuous wave pumped single-mode nanolasers in inorganic perovskites with robust stability and high quantum yield. *Nanoscale* **10**, 13565–13571 (2018).
S33. Wu ZY, Chen J, Mi Y et al. All-inorganic $CsPbBr_3$ nanowire based plasmonic lasers. *Adv Opt Mater* **6**, 1800674 (2018).
S34. Tiguntseva E, Koshelev K, Furasova A et al. Room-temperature lasing from mie-resonant nonplasmonic nanoparticles. *ACS Nano* **14**, 8149–8156 (2020).
S35. Cho S, Yang Y, Soljačić M et al. Submicrometer perovskite plasmonic lasers at room temperature. *Sci Adv* **7**, eabf3362 (2021).
S36. Safronov KR, Popkova AA, Markina DA et al. Efficient emission outcoupling from perovskite lasers into highly directional and long-propagation-length bloch surface waves. *Laser Photonics Rev* **16**, 2100728 (2022).
S37. Nezhad MP, Simic A, Bondarenko O et al. Room-temperature subwavelength metallo-dielectric lasers. *Nat Photonics* **4**, 395–399 (2010).
S38. Khajavikhan M, Simic A, Katz M et al. Thresholdless nanoscale coaxial lasers. *Nature* **482**, 204–207 (2012).
S39. Mylnikov V, Ha ST, Pan ZY et al. Lasing action in single subwavelength particles supporting supercavity modes. *ACS Nano* **14**, 7338–7346 (2020).
S40. Sung J, Shin D, Cho H et al. Room-temperature continuous-wave indirect-bandgap transition lasing in an ultra-thin WS_2 disk. *Nat Photonics* **16**, 792–797 (2022).